

Modal interference in optical nanofibers for sub-Angstrom radius sensitivity

FREDRIK K. FATEMI,^{1,*} JONATHAN E. HOFFMAN,² PABLO SOLANO,² ELIOT F. FENTON,² GUY BEADIE,³ STEVEN L. ROLSTON,² AND LUIS A. OROZCO²

¹Army Research Laboratory, Adelphi, Maryland 20783, USA

²Joint Quantum Institute, Department of Physics, University of Maryland and National Institute of Standards and Technology, College Park, Maryland 20742, USA

³Naval Research Laboratory, Washington, DC 20375, USA

*Corresponding author: fredrik.k.fatemi.civ@mail.mil

Received 30 September 2016; revised 23 November 2016; accepted 26 November 2016 (Doc. ID 277963); published 19 January 2017

Optical nanofibers (ONFs) of sub-wavelength dimensions confine light in modes with a strong evanescent field that can trap, probe, and manipulate nearby quantum systems. To measure the evanescent field and propagating modes and to optimize ONF performance, a surface probe is desirable during fabrication. We demonstrate a nondestructive near-field measurement of light propagation in ONFs by sampling the local evanescent field with a microfiber. This approach reveals the behavior of all propagating modes, and because the modal beat lengths in cylindrical waveguides depend strongly on the radius, it simultaneously provides exquisite sensitivity to the ONF radius. We show that our measured spatial frequencies provide a map of the average ONF radius (over a 600 μm window) along the 10 mm ONF waist with a 40 pm resolution and a high signal-to-noise ratio. The measurements agree with scanning electron microscopy (SEM) to within SEM instrument resolutions. This fast method is immune to polarization, intrinsic birefringence, mechanical vibrations, and scattered light and provides a set of constraints to protect from systematic errors in the measurements. © 2017 Optical Society of America

OCIS codes: (060.2310) Fiber optics; (350.4238) Nanophotonics and photonic crystals; (060.2270) Fiber characterization.

<https://doi.org/10.1364/OPTICA.4.000157>

1. INTRODUCTION

The evanescent fields outside optical nanofibers (ONFs) [1] allow strong interactions with the surrounding medium [2–7]. These waveguides have enabled several advances in quantum information technologies, including optical switches [8] and atom-mediated optical isolators [9,10], but have also facilitated fundamental experiments in nonlinear atom–light interactions [11], atom-number-resolving detection [12], electromagnetically induced transparency [13–16], and Bragg reflections from atoms [17,18].

The control achieved in the fabrication of high-transmission ONFs in both the fundamental mode [19] and higher-order modes [20,21] is excellent. A nondestructive tool to accurately measure the ONF radius and characterize the propagation of the modes is crucial for optimizing both fundamental and applied uses of ONFs. For example, the ONF radius, R , governs the coupling between a nearby atom (trapped or free) and the allowed nanofiber modes (see, e.g., Ref. [2]). These modes have distinct effective refractive indices (n_{eff}) that depend strongly on R . We can use modal beating to extract both the propagation properties and ONF geometry for optimizing atom-photon coupling. We recently examined propagation characteristics by imaging Rayleigh scattered (RS) light [22]. While RS is an effective tool for analyzing some propagation behavior, it uses far-field imaging and is hampered by excess

scattered light, mechanical vibrations of the ONF, and imaging resolutions so that only long-period modal beating can be cleanly resolved [22,23].

To circumvent the limitations of far-field imaging, contact techniques between an ONF and a microfiber probe have previously been used to measure the local radius variations of an ONF with sub-nanometer precision by propagating light through the microfiber probe and observing the mode spectrum of a whispering gallery or a composite photonic crystal cavity [24–27]. Though these approaches accurately measure ONF dimensions, they do not measure the propagation characteristics of the ONF. Other contact techniques rely on changes in the amplitude of light transmitted through the ONF. Sumetsky *et al.* used a standard fiber in contact with an ONF that detected sub-nanometer radius fluctuations by monitoring attenuation through the ONF [28]. These techniques can become sensitive to polarization and van der Waals forces, as in the recent work by Madsen *et al.* [29], and do not directly sample the modal composition of the local field.

In this work, we measure the beat lengths between propagating nanofiber modes in the near field over the ONF length through evanescent coupling to a microfiber probe. This near-field approach provides high ($\approx 1 \mu\text{m}$) longitudinal resolutions capable of measuring beating between any mode pairs and is immune

to excess scattered light and mechanical vibrations. The spatial frequencies are used to map the mean of the ONF radius to within 40 pm over 600 μm measurement windows along the ONF taper and waist. The amplitude of the beat frequency only enters in the signal-to-noise ratio of the resonance, which in this technique can be orders of magnitude better than those we obtained with Rayleigh scattering [22].

2. THEORETICAL CONSIDERATIONS

A standard optical fiber consists of a core of refractive index n_{core} and radius a , surrounded by a cladding with a lower refractive index n_{clad} and radius R . In our ONFs, R is reduced to sub-wavelength dimensions by a flame-brush technique [19]. At these dimensions, the ONF can be considered as a simple dielectric of index $n_{\text{ONF}} = n_{\text{clad}}$, surrounded by $n = 1.0$, as the original fiber core becomes negligible. The tapers connecting the standard fiber on the input and output side to the ONF waist have milliradian angles for adiabatic propagation [20].

Each ONF mode has a waveguide propagation constant, $\beta = kn_{\text{eff}}$, where k is the free-space propagation constant, $2\pi/\lambda$ (see Fig. 1 for the R dependence of n_{eff} and the spatial frequencies between specific mode pairs). n_{eff} decreases with R , as the evanescent field samples more of the surrounding lower-index medium; when n_{eff} equals the surrounding index, the mode reaches the cut-off and radiates out of the waveguide. Figure 1(a) shows n_{eff} for several modes in an ONF as a function of R . Because of the high index contrast ($\Delta n \simeq 0.5$), several modes are allowed even when $R = \lambda$. In this strong guiding regime, the scalar linearly polarized (LP) basis commonly used for standard optical fibers is replaced by a full vector mode basis, but for convenience, we still use the LP basis to group the modes into families. For example, the TE_{01} , TM_{01} , and two degenerate HE_{21} modes all belong to the LP_{11} mode family. The LP_{01} family has two degenerate HE_{11} modes,

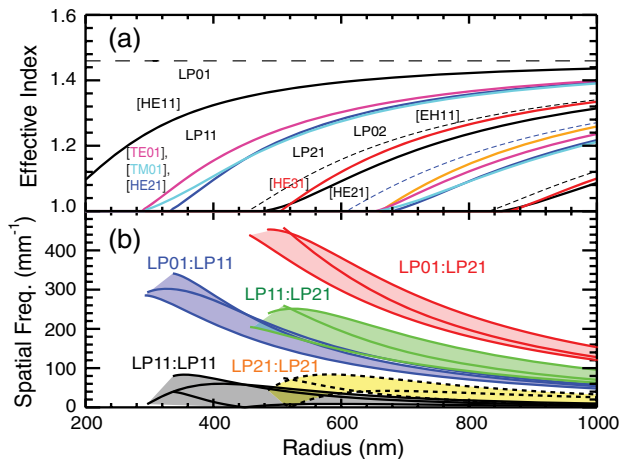


Fig. 1. Effective indices and spatial beating frequencies as a function of the fiber radius for the lowest modes in an ONF. (a) Effective indices of several allowed modes in an ONF with $n_{\text{ONF}} = 1.4534$, surrounded by $n = 1.0$, and a propagating wavelength of 795 nm. The first four families are labeled with the specific modes in brackets and are color-coded. (b) Spatial frequencies between mode pairs for the first three mode families. As a visual aid, all spatial frequencies between various mode families are colored the same way to show the groups of spatial frequencies observed at a particular R . Of the 9 beat frequency curves between LP_{11} and LP_{21} , only 3 are shown.

so that between the LP_{01} and LP_{11} families, there are 6 unique beat frequencies.

Two modes with different β_i and effective indices n_i will interfere with beat length $z_b = 2\pi/(\beta_i - \beta_j) = \lambda/(n_i - n_j)$, corresponding to a spatial frequency $\nu_b = 1/z_b = (n_i - n_j)/\lambda$. Figure 1(b) shows ν_b for several mode pairs in the lowest four mode families with groups of curves shaded according to which families are involved. As R decreases, the curves end abruptly when one of the modes reaches the cutoff. Near the cutoffs, interfamily beating is restricted to $z_b < 5 \mu\text{m}$ ($\nu_b > 200 \text{ mm}^{-1}$) (e.g., between the LP_{01} and LP_{11} families), while for intrafamily beating, $z_b > 10 \mu\text{m}$ ($\nu_b < 100 \text{ mm}^{-1}$). Our previous RS results [22] were limited to intrafamily beating because of excess scattering and mechanical vibrations, but the near-field approach demonstrated here can measure beating between any modes in fused silica.

3. EXPERIMENT

The ONFs are drawn to design radii of 390 nm that support the LP_{01} and LP_{11} mode families. We use a stable diode laser with $\lambda = 794.98 \text{ nm} \pm 0.01 \text{ nm}$ (Vescent D2-100-DBR) to launch superpositions of all 6 modes in the LP_{01} and LP_{11} families [20] so beat frequencies between all possible pairs of propagating modes can be observed on the waist.

To detect the propagating light, we use a fiber probe with 6- μm -diameter waist that contacts the ONF from below with a crossing angle of 67 deg, as drawn in Fig. 2(a). Figure 2(b) shows an image of the probe fiber in contact with the ONF. The ONF has a taper angle $\Omega = 1 \text{ mrad}$, a design waist $R_w = 390 \text{ nm}$, and a waist length $L = 10 \text{ mm}$. At $R_w = 390 \text{ nm}$, the waist supports all modes in the LP_{01} and LP_{11} families at $\lambda = 795 \text{ nm}$. A small crossing angle would provide excellent optical coupling to the probe fiber but would decrease the spatial resolution; a large crossing angle improves the spatial resolution but reduces optical coupling to propagating modes of the probe fiber. Our crossing angle is a compromise between these issues and restrictions due to optical mounts and the apparatus. The probe fiber is a standard, single-mode SM750 optical fiber tapered in the same pulling apparatus. Because this probe fiber is highly multimode in the waist, only a small percentage of the evanescently coupled light reaches the detector, which measures only the light guided in the probe fiber core. For our ONF, crossing angle, and probe fiber, the power detected is typically $10^{-5} - 10^{-6}$ of the power propagating in the ONF waist (1–2 mW) for the modes of interest. The choice of probe radius is also governed by practical considerations: a smaller probe fiber would more efficiently collect light and have a higher spatial resolution if needed, but it would have poor mechanical stability. The probe fiber is kept under tension so fluctuations that could arise due to multimode interference are not observed.

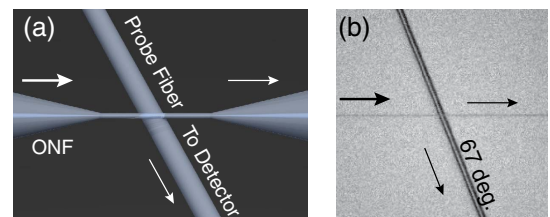


Fig. 2. (a) Schematic of probe fiber with respect to ONF. (b) Camera image of probe fiber and nanofiber on the ONF waist.

The contact point is translated at 20 $\mu\text{m/s}$ over the ONF length (and is sampled every 20 nm) by the same high-resolution stepper motors used during ONF fabrication to measure the propagation behavior in the ONF. Although this approach could lead to scratches on the ONF [25] or mechanical vibrations, we monitored the transmitted power and intensity distribution and saw no degradation or transient effects indicating either one. We have found that speeds slower than this can result in discontinuous signals due to stick-slip between the two fibers, but the ideal speed depends also on the crossing angle and tension.

4. RESULTS

A. Propagation Behavior

Figure 3 shows the detected light as a function of the propagation distance (z) along the fiber. Figure 3(a) shows the detected power from about 15 mm before the center of the waist on the input taper and continues to 15 mm onto the output taper. The origin of the x -axis is the middle of the approximately 10-mm-long waist L . We choose this origin because the taper is nominally symmetric, making comparisons between the modal distribution in the input and output tapers apparent.

Several properties of the light propagation can be observed in Fig. 3. Because the field in the ONF is evanescently coupled to the probe fiber, the signal amplitude in Fig. 3(a) is largest on the waist ($|z| \leq 5$ mm). The detected power is significantly greater and more heavily structured on the input taper ($z < -5$ mm) than on the output taper ($z > 5$ mm), where the average signal amplitude smoothly decays with clean oscillations. This asymmetry is due to the nonadiabaticity of the pull, causing excitation of higher-order modes when the light guidance transitions from core-cladding guidance to cladding-air guidance. On the input taper, these higher-order modes reach the cutoff, eventually leaving only LP_{01} and LP_{11} to interfere on the waist and output taper. This leads to fewer observed beat frequencies, shown in the region from $z = 4$ –8 mm of Fig. 3(b). Figures 3(b)–3(d) show successively narrower ranges of data near the output of the waist, with two beat length scales apparent in Fig. 3(d). The shorter length scale, with $z_b < 5$ μm , is due to interference between the LP_{01} and LP_{11} modes; the structure with $z_b \simeq 60$ μm is due to intra-modal interference between members of the LP_{11} family.

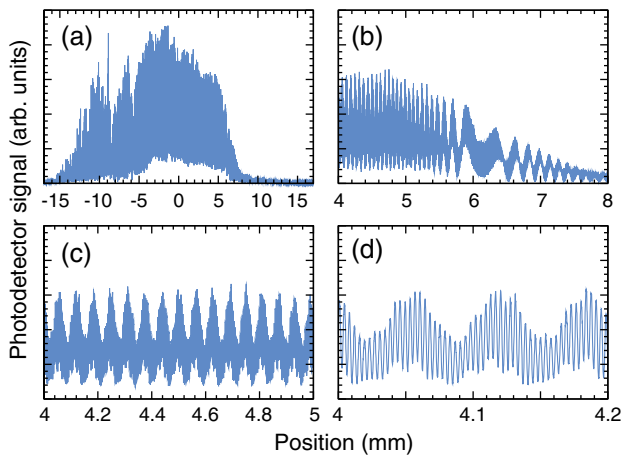


Fig. 3. (a) Near-field scanning probe signals over about 30 mm of the ONF. The waist is between $|z| \leq 5$ mm. (b)–(d) Successive magnifications on the output side of the waist.

B. Spectrogram Analysis

We quantify the spatial frequencies and identify participating modes using a spectrogram analysis [22,30]. Briefly, we Fourier transform the signals measured in Fig. 3(a) with a sliding window of 6.0 μm width to calculate the local beat frequencies as a function of z . Figure 4(a) depicts the design profile for the fiber, and Fig. 4(b) shows the resulting spectrogram.

Each curve in Fig. 4(b) is due to the interference of two modes. On the input side ($z < -5$ mm), the complicated spatial structure observed in Fig. 3(a) is decomposed into numerous curves. Far from the waist, each curve begins with both a low amplitude and a low spatial frequency. The curves are less visible because in these regions, most of the field is in the ONF, so the evanescent field is small. Also, the effective indices far from the cutoff are all approximately n_{ONF} , so the beat frequencies are low.

Closer to the waist, the curve amplitudes and spatial frequencies increase. Most of the curves abruptly end, similar to the calculations shown in Fig. 1(b). We show in Fig. 4(b) a number of calculated curves superimposed on the spectrogram to estimate R . To label the unknown curves, we first determined the local R as a function of z using a single known spectrogram curve ($\text{HE}_{11}\text{:TM}_{01}$) and the calculations of Fig. 1(b). The right axis shows this conversion. Using this $R(z)$, other mode pairs can be identified by comparison to Fig. 4(b). The shortest visible beat lengths $z_b \simeq 2.0$ μm ($\nu_b \simeq 500$ mm^{-1}) are close to the shortest observable in fused silica, which is $z_b \simeq 2\lambda \simeq 1.6$ μm ($\nu_b \simeq 625$ mm^{-1}).

On the waist, only the fundamental LP_{01} (one mode) and first higher-order LP_{11} (three modes) mode families can propagate, and the observed spatial frequencies are approximately constant. With these two mode families, there are 6 observable and

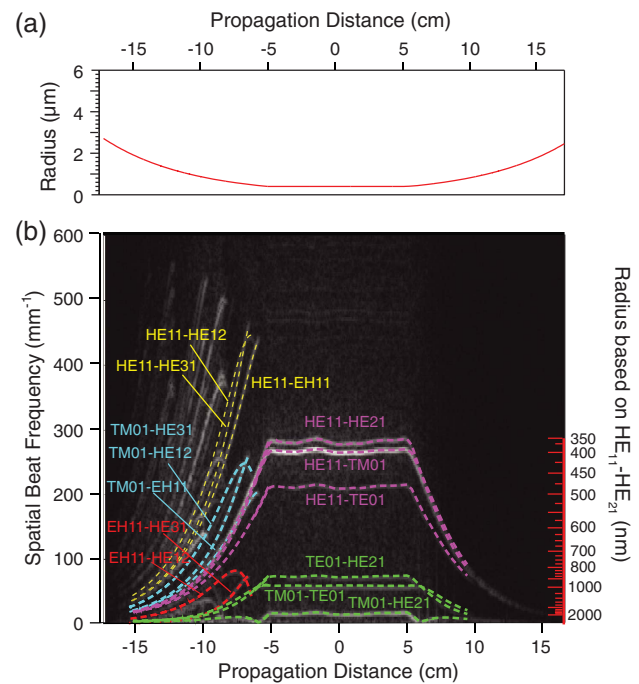


Fig. 4. (a) Design profile for ONF as a function of the propagation distance. (b) Spectrograms of the data, along with calculated beat-frequency curves for a number of mode pairs as a function of the propagation distance. Curves of the same color belong to the same family. The right axis on (b) shows the extracted radius corresponding to the $\text{HE}_{11}\text{:TM}_{01}$ curve.

nondegenerate pairs of interfering modes on the waist (other faint features near 500 mm^{-1} on the waist are due to aliasing artifacts). The fundamental HE_{11} mode interferes with the three nondegenerate modes of the LP_{11} family with spatial frequencies near $\nu_b = 300 \text{ mm}^{-1}$. Three additional frequencies below $\nu = 100 \text{ mm}^{-1}$ occur due to interference between the modes within the LP_{11} family. The lowest frequency curve, corresponding to the $\text{TM}_{01}:\text{HE}_{21}$ interference, shows a zero crossing at $|z| = 6 \text{ mm}$, evident in the calculated curves shown in Fig. 1(b) near $R = 450 \text{ nm}$.

The observed $\text{TE}_{01}:\text{TM}_{01}$ interference, occurring at the difference frequency between the $\text{TE}_{01}:\text{HE}_{21}$ and $\text{TM}_{01}:\text{HE}_{21}$ curves, is surprising, as these two modes are orthogonal everywhere and their individual modal powers are constant. In the Rayleigh scattering results of Ref. [22], we observed no beating between these two modes for this reason. However, because our probe fiber is highly multimode at the point of contact with an oblique crossing angle, these two orthogonal modes can couple to the same set of probe fiber modes, including the fundamental mode. Thus, the relative phase between the TE_{01} and TM_{01} modes that are evanescently coupled will affect the amount of light that reaches the detector, where the fiber is single mode, even though the strength of the evanescent field does not change. Only a small amount of cross-coupling needs to occur for these interference effects to be noticeable.

C. Fiber Radius

The beat length varies particularly steeply with R near the mode cutoffs [Figs. 1(b) and 4(b)]. This property can be used to determine $R(z)$ with high precision. Figure 5 shows $d\nu_b/dR$ for each of the allowed mode pairs on the waist, at $\lambda = 795 \text{ nm}$. The sensitivity is particularly strong for the $\text{HE}_{11}:\text{LP}_{01}$ curves (solid lines), with the $\text{HE}_{11}:\text{HE}_{21}$ curve achieving $d\nu_b/dR = -1 \text{ mm}^{-1}/\text{nm}$ and the $\text{HE}_{11}:\text{TM}_{01}$ curve achieving $d\nu_b/dR = -0.7 \text{ mm}^{-1}/\text{nm}$ at $R = 400 \text{ nm}$. Conversely, ν_b is insensitive to R for the $\text{TM}_{01}:\text{TE}_{01}$ pair near $R = 420 \text{ nm}$ and the $\text{TE}_{01}:\text{HE}_{21}$ pair near $R = 360 \text{ nm}$. The spectrogram in Fig. 4(b) shows these characteristics clearly in the waist region of this ONF, which had a design radius of $R = 390 \text{ nm}$: The observed fluctuations in the beat frequency are strongest for the $\text{HE}_{11}:\text{HE}_{21}$ curve, while the $\text{TM}_{01}:\text{TE}_{01}$ curve is constant. At larger R , other mode pairs can be used for high sensitivity.

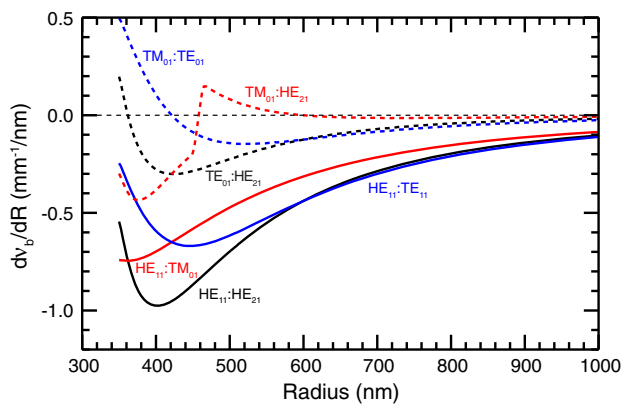


Fig. 5. Rate of change of the beat frequency with fiber radius. Note that the $\text{HE}_{11}:\text{HE}_{21}$, $\text{HE}_{11}:\text{TE}_{01}$, and $\text{HE}_{11}:\text{TM}_{01}$ have high sensitivities to the radius near 400 nm .

We can find not only the value of R at a given point but map its local variations with high precision on the waist. To do this, we determine the central frequencies of the features in each $600\text{-}\mu\text{m}$ -long fast Fourier transform (FFT) window comprising the spectrogram as in Fig. 6. Over this window size, which is smaller than the flame diameter used for heating the fiber, the beat frequencies are relatively constant and the spectral features are transform limited. Following the spectroscopic rule that the center of a resonance can be determined by its full width at half-maximum (FWHM) divided by the signal-to-noise ratio in the unfiltered data [31] (blue trace of Fig. 6), we estimate that the $\text{HE}_{11}:\text{TM}_{01}$ beat note near 265 mm^{-1} has an FWHM of 0.5 mm^{-1} with a signal-to-noise ratio better than 80. This estimate gives an uncertainty in the resonance center less than 0.01 mm^{-1} and an uncertainty in R of $\approx 0.01 \text{ nm}$. The origin of the noise in Figs. 6–8 is largely from the stick-slip between the probe fiber and ONF, which causes phase discontinuities and electronic noise. Optical noise from bulk Rayleigh scattering inside the ONF has negligible coupling into the single mode of the probe fiber.

Having determined an estimate for the resolution of the method, we now proceed in a more quantitative way: the centers of the transform-limited features in discrete FFTs can be accurately found by applying a mild Gaussian windowing function to the data ($1/e^2 = 400 \mu\text{m}$) prior to calculating the FFT [32] (red trace in Fig. 6). This broadens the spectral features to a known Gaussian form that can easily be fitted. Applying this approach to the $\text{HE}_{11}:\text{TM}_{01}$ curve, we find that the beat frequencies on the waist of the ONF vary from $271.13 \pm 0.03 \text{ mm}^{-1}$ to $265.56 \pm 0.03 \text{ mm}^{-1}$, corresponding to radii $R = 394.85 \pm 0.04 \text{ nm}$ to $R = 404.29 \pm 0.04 \text{ nm}$ over the 10 mm waist, where the uncertainty reflects 95% confidence windows on the Gaussian fitting function using a $600\text{-}\mu\text{m}$ -long FFT window.

We verified the accuracy of the method using scanning electron microscopy (SEM). Figure 7 shows the lower part of the spectrum of spatial frequencies for another ONF that could then be destroyed in the SEM. Note that only two of the three marked beat frequencies are independent, with $\nu(\text{TM}_{01}:\text{HE}_{21}) + \nu(\text{TM}_{01}:\text{TE}_{01}) = \nu(\text{TE}_{01}:\text{HE}_{21})$. The $\text{TE}_{01}:\text{HE}_{21}$ beat frequency, with a signal-to-noise ratio close to 10, gives an estimate of the fiber diameter of $742 \pm 0.3 \text{ nm}$. This value is within the bounds measured by the SEM of $740 \pm 6 \text{ nm}$. This fiber probe

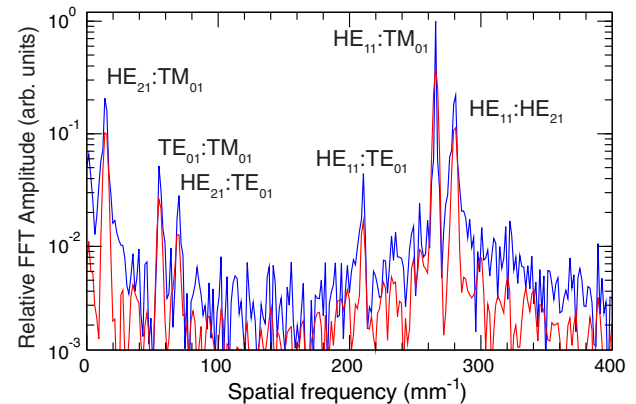


Fig. 6. FFT of a $600 \mu\text{m}$ long segment of the data (waist of the ONF in Fig. 4). Note the logarithmic vertical scale. The blue trace is the raw data, and the red has been multiplied by a Gaussian filter (see text for details).

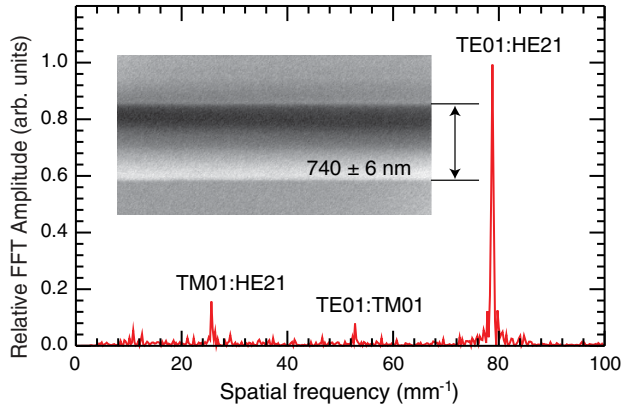


Fig. 7. Beat frequencies for the ONF shown in the inset SEM image. The low spatial frequency beat frequencies correspond to a fiber diameter of 742 ± 0.3 nm, in agreement with the SEM measurement of 740 ± 6 nm.

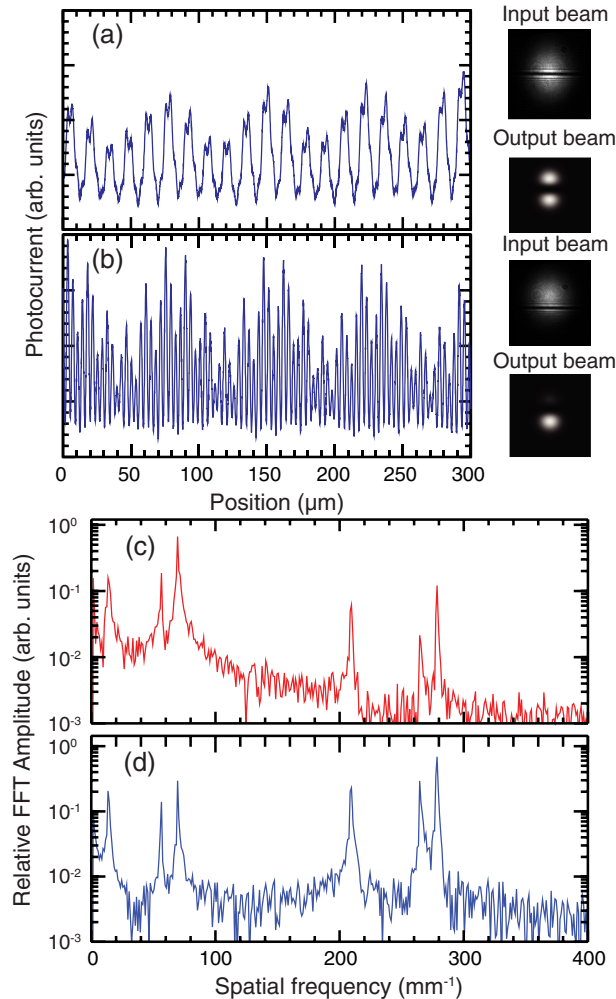


Fig. 8. Control of the modes beating at the fiber waist. (a) shows the spatial data when the HE_{11} mode is suppressed. (b) shows the spatial data when the HE_{11} is present. The two photos to the right of (a) and (b) show the intensity profiles at the fiber input (top) and output (bottom) for the appropriate modes. (c) and (d) show the FFT of the 300 μm long spatial scan at the waist of the ONF. Note the logarithmic vertical scale. The dark line in the input beam pictures is caused by the π phase jump on the phase plate.

measurement is at least an order of magnitude more precise than the SEM and is also nondestructive.

D. Mode Control

This evanescent probe technique can spatially resolve high-frequency interfamily mode beating. The amplitude of the beating is proportional to the product of two mode amplitudes. We can control the relative strengths of any pair of desired modes on the waist by looking at the magnitude of their beat note in the Fourier transform. We demonstrate one use of the technique to evaluate the relative weight of the fundamental mode family propagating on the ONF waist in Fig. 8. Relative weights of the LP_{01} and LP_{11} families are controlled by inserting a π -phase plate into the input Gaussian beam [30]. Without a phase plate, well-aligned fiber coupling of the input Gaussian beam has a maximum overlap with the LP_{01} mode, whereas a centered plate ideally has only an LP_{11} contribution. Mixtures of these families are produced by decentering the plate [intensity distributions at the fiber input and output are next to Figs. 8(a) and 8(b)]. Figures 8(a) and 8(b) show two traces over the same section of the ONF, with their respective FFTs on the bottom [Figs. 8(c) and 8(d)], when a phase plate is used to control the relative amount of LP_{11} and LP_{01} modal content within the ONF. Figure 8(a) is the raw oscilloscope data when the fundamental mode is reduced by centering a π -phase plate in the input beam. The peaks above 200 mm^{-1} , due to the LP_{01} : LP_{11} beating, are smaller than the intramodal LP_{11} : LP_{11} beating. When the phase plate is shifted down [input picture next to Fig. 8(b)] so the beam has a mixture of fundamental and higher modes, all 6 peaks in the FFT are strong. The highest beat frequencies at almost 300 mm^{-1} correspond to beating with the fundamental HE_{11} mode, producing oscillations with $z_b \approx 3.57 \mu\text{m}$, close to the theoretical limit of 2λ for silica ONFs, something impossible to resolve with Rayleigh scattering [22]. The absolute weights of the various mode strengths would require the calibration of the coupling of each propagating mode.

5. DISCUSSION AND CONCLUSIONS

As R increases, numerous inter- and intrafamily spatial frequencies can be observed and identified using this near-field scanning approach with sub-micron beat-length resolution. This resolution is high enough to measure the minimum possible $z_b = \lambda/(n_{\text{ONF}} - 1) \approx 2\lambda = 1.6 \mu\text{m}$ for this work with $n = 1.4534$ and our propagating $\lambda = 794.98 \text{ nm}$. The main limitation of the method comes from the requirement of an allowed higher-order mode family to provide measurable beat frequencies. A single-mode operation occurs when $R \leq 0.363\lambda$ (V -number = 2.405), making measurements of $R < 100 \text{ nm}$ impractical because of the short optical wavelengths required.

Good agreement with all beat frequency curves can only be satisfied for the correct value of n . We used the experimentally obtained frequencies for one of the beat frequencies (HE_{11} : TE_{01}) to extract $R(z)$ based on that curve. We then used these radii to calculate the 5 other curves. An incorrect value of n results in poor agreement; one cannot compensate for an incorrect value of n by adjusting R . For a fixed value of R and a set of beat frequencies with uncertainties, as in Fig. 6, of 0.03 mm^{-1} , the data are consistent only as long as the index agrees to within 2×10^{-4} [33]. The dispersion curve of fused silica is typically quoted to an accuracy 1×10^{-5} . This self-consistency check strongly suppresses any systematic effects in the procedures to either extract the radius

or study the propagation of the higher-order modes in the ONF. The analysis is unaffected by uncertainties in laser wavelength at the ± 0.01 nm uncertainty of our diode laser. It would take a wavelength error in excess of 0.2 nm to induce beat frequency shifts greater than the observed uncertainties.

The technique presented here has a high signal-to-noise ratio, which allows high spatial resolutions. It does this with immunity to scattered light and ONF mechanical stress and vibrations. The mode-dependent coupling from the ONF to the probe fiber conditions the amplitudes of the beat resonances but does not change the frequency of the beating. The amplitudes then give only qualitative information about the coupling. The average radius with its sub-nanometer resolution comes from the beating frequency, and shows robustness and repeatability, while the scanning *in situ* is fast. The analysis of the transmission properties for higher-order modes and their cutoffs give unique protection against systematic errors. The excellent spatial resolution in the radius determination can aid in evaluating the uniformity of the pulled fiber (e.g., the noticeable variation in R in the test fiber of Fig. 3) and can be used to optimize ONF production.

Funding. Army Research Office (ARO) (528418); National Science Foundation (NSF) (PHY-1430094); Defense Advanced Research Projects Agency (DARPA) (HR0011411122); Office of Naval Research (ONR).

Acknowledgment. We thank Je-Hyung Kim for his help with the SEM imaging.

REFERENCES

1. L. Tong, R. R. Gattass, J. B. Ashcom, S. He, J. Lou, M. Shen, I. Maxwell, and E. Mazur, "Subwavelength-diameter silica wires for low-loss optical wave guiding," *Nature* **426**, 816–819 (2003).
2. F. L. Kien, S. D. Gupta, V. I. Balykin, and K. Hakuta, "Spontaneous emission of a cesium atom near a nanofiber: Efficient coupling of light to guided modes," *Phys. Rev. A* **72**, 032509 (2005).
3. M. J. Morrissey, K. Deasy, M. Frawley, R. Kumar, E. Prel, L. Russell, V. G. Truong, and S. Nic Chormaic, "Spectroscopy, manipulation and trapping of neutral atoms, molecules, and other particles using optical nanofibers: a review," *Sensors* **13**, 10449–10481 (2013).
4. R. Yalla, F. L. Kien, M. Morinaga, and K. Hakuta, "Efficient channeling of fluorescence photons from single quantum dots into guided modes of optical nanofiber," *Phys. Rev. Lett.* **109**, 063602 (2012).
5. M. Fujiwara, K. Toubaru, T. Noda, H.-Q. Zhao, and S. Takeuchi, "Highly efficient coupling of photons from nanoemitters into single-mode optical fibers," *Nano Lett.* **11**, 4362–4365 (2011).
6. S. T. Dawkins, R. Mitsch, D. Reitz, E. Vetsch, and A. Rauschenbeutel, "Dispersive optical interface based on nanofiber-trapped atoms," *Phys. Rev. Lett.* **107**, 243601 (2011).
7. E. Vetsch, D. Reitz, G. Sagué, R. Schmidt, S. T. Dawkins, and A. Rauschenbeutel, "Optical interface created by laser-cooled atoms trapped in the evanescent field surrounding an optical nanofiber," *Phys. Rev. Lett.* **104**, 203603 (2010).
8. D. O'shea, C. Junge, J. Volz, and A. Rauschenbeutel, "Fiber-optical switch controlled by a single atom," *Phys. Rev. Lett.* **111**, 193601 (2013).
9. R. Mitsch, C. Sayrin, B. Albrecht, P. Schneeweiss, and A. Rauschenbeutel, "Quantum state-controlled directional spontaneous emission of photons into a nanophotonic waveguide," *Nat. Commun.* **5**, 5713 (2014).
10. J. Petersen, J. Volz, and A. Rauschenbeutel, "Chiral nanophotonic waveguide interface based on spin-orbit interaction of light," *Science* **346**, 67–71 (2014).
11. S. M. Spillane, G. S. Pati, K. Salit, M. Hall, P. Kumar, R. G. Beausoleil, and M. S. Shahriar, "Observation of nonlinear optical interactions of ultralow levels of light in a tapered optical nanofiber embedded in a hot rubidium vapor," *Phys. Rev. Lett.* **100**, 233602 (2008).
12. J.-B. Béguin, E. M. Bookjans, S. L. Christensen, H. L. Sørensen, J. H. Müller, E. S. Polzik, and J. Appel, "Generation and detection of a sub-Poissonian atom number distribution in a one-dimensional optical lattice," *Phys. Rev. Lett.* **113**, 263603 (2014).
13. C. Sayrin, C. Clausen, B. Albrecht, P. Schneeweiss, and A. Rauschenbeutel, "Storage of fiber-guided light in a nanofiber-trapped ensemble of cold atoms," *Optica* **2**, 353–356 (2015).
14. B. Gouraud, D. Maxein, A. Nicolas, O. Morin, and J. Laurat, "Demonstration of a memory for tightly guided light in an optical nanofiber," *Phys. Rev. Lett.* **114**, 180503 (2015).
15. D. E. Jones, J. D. Franson, and T. B. Pittman, "Ladder-type electromagnetically induced transparency using nanofiber-guided light in a warm atomic vapor," *Phys. Rev. A* **92**, 043806 (2015).
16. R. Kumar, V. Gokhroo, and S. N. Chormaic, "Multi-level cascaded electromagnetically induced transparency in cold atoms using an optical nanofiber interface," *New J. Phys.* **17**, 123012 (2015).
17. H. L. Sørensen, J.-B. Béguin, K. W. Kluge, I. Iakoupov, A. S. Sørensen, J. H. Müller, E. S. Polzik, and J. Appel, "Coherent backscattering of light off one-dimensional atomic strings," *Phys. Rev. Lett.* **117**, 133604 (2016).
18. N. V. Corzo, B. Gouraud, A. Chandra, A. Goban, A. S. Sheremet, D. V. Kupriyanov, and J. Laurat, "Large Bragg reflection from one-dimensional chains of trapped atoms near a nanoscale waveguide," *Phys. Rev. Lett.* **117**, 133603 (2016).
19. J. E. Hoffman, S. Ravets, J. Grover, P. Solano, P. R. Kordell, J. D. Wong-Campos, S. L. Rolston, and L. A. Orozco, "Ultrahigh transmission optical nanofibers," *AIP Adv.* **4**, 067124 (2014).
20. S. Ravets, J. E. Hoffman, L. A. Orozco, S. L. Rolston, G. Beadie, and F. K. Fatemi, "A low-loss photonic silica nanofiber for higher-order modes," *Opt. Express* **21**, 18325–18335 (2013).
21. M. C. Frawley, A. Petcu-Colan, V. G. Truong, and S. Nic Chormaic, "Higher order mode propagation in an optical nanofiber," *Opt. Commun.* **285**, 4648–4654 (2012).
22. J. E. Hoffman, F. K. Fatemi, G. Beadie, S. L. Rolston, and L. A. Orozco, "Rayleigh scattering in an optical nanofiber as a probe of higher-order mode propagation," *Optica* **2**, 416–423 (2015).
23. M. Szczurkowski, W. Urbanczyk, M. Napiorkowski, P. Hlubina, U. Hollenbach, H. Sieber, and J. Mohr, "Differential Rayleigh scattering method for measurement of polarization and intermodal beat length in optical waveguides and fibers," *Appl. Opt.* **50**, 2594–2600 (2011).
24. T. A. Birks, J. C. Knight, and T. E. Dimmick, "High-resolution measurement of the fiber diameter variations using whispering gallery modes and no optical alignment," *IEEE Photon. Technol. Lett.* **12**, 182–183 (2000).
25. M. Sumetsky and Y. Dulashko, "Radius variation of optical fibers with Angstrom accuracy," *Opt. Lett.* **35**, 4006–4008 (2010).
26. Y. Semenova, V. Kavungal, Q. Wu, and G. Farrell, "Submicron accuracy fiber taper profiling using whispering gallery modes in a cylindrical fiber micro-resonator," *Proc. SPIE* **9634**, 96343F (2015).
27. J. Keloth, M. Sadgrove, R. Yalla, and K. Hakuta, "Diameter measurement of optical nanofibers using a composite photonic crystal cavity," *Opt. Lett.* **40**, 4122–4125 (2015).
28. M. Sumetsky, Y. Dulashko, J. M. Fini, A. Hale, and J. W. Nicholson, "Probing optical microfiber nonuniformities at nanoscale," *Opt. Lett.* **31**, 2393–2395 (2006).
29. L. S. Madsen, C. Baker, H. Rubinsztein-Dunlop, and W. P. Bowen, "Non-destructive imaging of optical nanofibers," *arXiv:1606.04064* (2016).
30. S. Ravets, J. E. Hoffman, P. R. Kordell, J. D. Wong-Campos, S. L. Rolston, and L. A. Orozco, "Intermodal energy transfer in a tapered optical fiber: optimizing transmission," *J. Opt. Soc. Am. A* **30**, 2361–2371 (2013).
31. A. Clairon, C. Salomon, S. Guellati, and W. D. Phillips, "Ramsey resonance in a Zacharias fountain," *Europhys. Lett.* **16**, 165–170 (1991).
32. M. Gasior and J. L. Gonzalez, "Improving FFT frequency measurement resolution by parabolic and Gaussian spectrum interpolation," *AIP Conf. Proc.* **732**, 276–285 (2004).
33. I. H. Malitson, "Interspecimen comparison of the refractive index of fused silica," *J. Opt. Soc. Am.* **55**, 1205–1209 (1965).